SIMULATION OF THE AIRFLOW INSIDE A HYBRID DRYER

Cristiana Brasil Maia [1,*], André Guimarães Ferreira[2], Luben Cabezas-Gómez[1], Sérgio de Morais Hanriot[1] & Tiago de Oliveira Martins[1]

[1] Pontifical Catholic University of Minas Gerais, Av. Dom José Gaspar, 500. 30535-970, Brazil

[2] Federal Center of Technological Education of Minas Gerais. Av. Amazonas, 5253. 30480-000. Brazil

ABSTRACT

Food is the basic comfort and necessity of living beings. The major problem faced by the mankind is the balance of food production and consumption. About 25% of the world food production is lost between the producer and the consumer. The world's food problem could be appeased reducing the food losses that occur mainly due to failures on the production storage and transportation. The food preservation is the only method to reduce food losses and drying is the method that is being adopted since many centuries. This paper presents a numerical simulation of the airflow inside a hybrid solar-electrical dryer, using a commercial CFD package. With prescribed temperatures and velocities, the model predicts the behavior of the airflow inside the device. Numerical results are compared with experimental data.

Keywords: *Hybrid dryer, Numerical simulation, CFX*

1. INTRODUCTION

Drying is an essential process used all over the world for the preservation of farm produce. It helps in reducing the water activity of the produce to a level below which deterioration doesn't occur for a definite duration [1]. The drying process helps to achieve better product quality, longer safe storage period and reduction in post-harvest losses. The reduction in post-harvest losses ensures more food availability for growing world population [2]. Various drying methods are employed to dry different food produce. Natural sun drying is probably the oldest method to food preservation. However, it has several drawbacks, such as difficulty to control the rate of drying, insect infestation and microbial contamination. Replacing natural sun drying by artificial drying or by solar drying can significantly reduce these drawbacks and the losses caused by them [3]. Nevertheless, the drying air characteristics in solar dryers depend on ambient conditions, what can reduce the final product's quality [4]. Artificial drying requires higher operational costs, what can be unfeasible to some applications [5]. In this context, hybrid solar dryers arise as an interesting solution [6]. The characteristics of the drying air can be controllable, improving the quality of dried products and the drying costs can be reduced, comparing with artificial drying.

Many solar food dryers have been developed over the past few years, yielding varying degrees of technical performance. Fudholi *et. al.* [7] divide the solar dryer into four types: direct solar dryers, indirect solar dryers, mixed-mode dryers and hybrid solar dryers. The authors present a review of these types of solar dryers with aspect to the product being dried, technical and economical aspects. The technical directions in the development of solar-assisted drying systems for agricultural produce are compact collector design, high efficiency, integrated storage, and long-life drying system..

In hybrid dryers, the drying process is not so dependable of the incident solar radiation, since an auxiliary source of energy can be used to maintain the drying conditions uniform. A prototype of an indirect active hybrid solar-electrical dryer was built and tested in Ouargla (South-east Algeria) by [8]. Drying tests of tomato slices were performed. The authors observed that when the airflow rates of the drying air increase the percent energy contribution by the solar air heater decreased and the percent energy contribution of the auxiliary heater increased. This increase is due to the collector outlet temperature of the air drying which will be decreased significantly in high airflow rates.

The prediction of the airflow inside the dryer helps to design most suitable geometric configurations of the device, improving the drying process. Numerical techniques have been used to numerically model the behaviour of the airflow inside several kinds of dryers [9-14]. The present paper presents the numerical simulation of the airflow inside a hybrid solar-electrical dryer, performed with the ANSYS-CFX Code. The numerical results of velocity and temperature of the airflow were compared with experimental data obtained in a prototype.

2. EXPERIMENTAL SETUP

A hybrid solar dryer was designed, constructed and tested in Belo Horizonte (Brazil), with latitude and longitude of 20°S and 43.5°W, respectively. The dryer consists mainly of a solar chamber and a drying chamber. A schematic view of the dryer is shown in Fig. 1. The upper surface of the solar chamber is made of glass. Solar radiation passes trough this surface and reaches the lower surface – the solar collector. Since the solar collector is black, it absorbs

most of the incident solar radiation, attaining high temperatures. The walls of the solar chamber were built with galvanized steel plates, painted in black, thermally insulated with wool glass and covered with galvanized steel plates painted in green. The solar chamber is opened at its edges, with 1.70 m of length, 1.20 m of width and 0.35 m of internal height. It is inclined at 30° from horizontal, in order to maximize the absorption of solar radiation during the winter. The solar chamber is covered with glass.

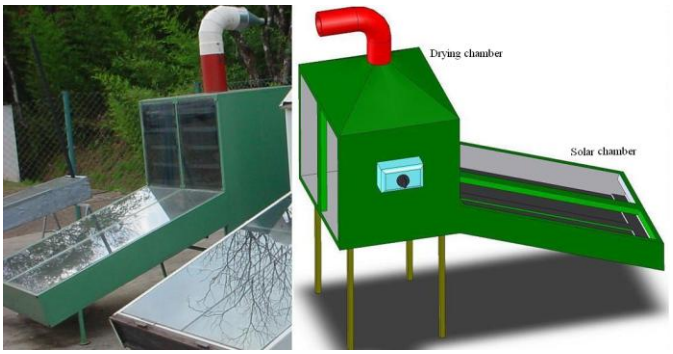

Figure 1. Hybrid solar-electrical dryer.

The drying chamber has 0.85 m of length, 1.20 m of width and 1.05 m of height. It was built using galvanized steel plates, thermally insulated with wool glass and covered with galvanized steel plates painted in green. The frontal face of solar chamber is covered with glass. To allow the drying air exit, a 0.20m diameter chimney (with an exhauster) was installed on the top of the dryer. Ten trays (0.74 m x 0.52 m) were put inside the drying chamber, corresponding to an area of 3.85m^2. The products can be introduced and removed trough two doors, located on the back of the dryer. A thermostat was installed in the chimney to control the airflow temperature in the device outlet. An auxiliary heating air resistance (2400 W), used to complement the solar energy, was installed on the bottom of the drying chamber.

Incoterm thermocouples were used to measure ambient temperature, the drying air temperature inside the dryer and the temperature of the walls. In the range of operation from -20°C to 150°C, the uncertainties of the sensors are 2.0°C. The velocity of drying air was measured with a 0.050 m diameter propeller anemometer (Homis), with a global uncertainty of 6%. Uncertainties of the measurement devices were obtained to a 95% level of confidence, according to [15]. A metrological analysis was performed to minimize measurement errors. All these data were measured three times to reduce measurement uncertainties.

3. MATHEMATICAL MODEL

The numerical simulations are performed using the Reynolds-Averaged Navier-Stokes (RANS) equations. The continuity, momentum and energy equations were solved with κ-ω SST (Shear Stress Transport) turbulence model, proposed by [16] from the *k-ω* turbulence model, initially formulated by [17]. Other turbulence models were tested and the κ-ω SST was the one that best fitted experimental data. The Boussinesq approximation was used for thermal buoyancy. A grid independence solution analysis was performed, in order to find the correct mesh size as a compromise between accuracy and computational cost. The numerical simulations were performed using the ANSYS-CFX 11 software package, which is a general purpose CFD package that includes a solver based on the finite volumes method for structured and unstructured grids.

The mass, momentum and energy conservation equations are given in a general form by:

$$\frac{\partial \rho}{\partial t} + \vec{\nabla} \cdot (\rho U) = 0 \tag{1}$$

$$\frac{\partial (\rho U)}{\partial t} + \vec{\nabla} \cdot (\rho U \otimes U) = -\vec{\nabla} p' + \vec{\nabla} \cdot \left(\mu_{eff} (\vec{\nabla} U)\right) + B \tag{2}$$

$$\frac{\partial (\rho h_{tot})}{\partial t} - \frac{\partial p}{\partial t} + \vec{\nabla} \cdot (\rho U h_{tot}) = +\vec{\nabla} \cdot \left(k(\vec{\nabla} T)\right) + S_E \tag{3}$$

In the above equations, B is the sum of body forces, μ_{eff} is the effective viscosity accounting for turbulence, and p' is the modified pressure, given respectively by:

$$\mu_{eff} = \mu + \mu_t \tag{4}$$

$$p' = p + \frac{2}{3}\rho k \tag{5}$$

h_{tot}, p and k represent the total specific enthalpy, the pressure and the thermal conductivity and S_E is the energy equation source term. The total specific enthalpy is related to the thermodynamic specific enthalpy h by:

$$h_{tot} = h + \frac{1}{2}U^2 \tag{6}$$

In this paper the effects of turbulence are considered using the *SST* (Shear Stress Transport) turbulence model. The model was proposed by [16] and grew from the denominated baseline *k-ω* model [18]. The baseline *k-ω* model makes use of the *k-ε* model in regions far away from the walls and the *k-ω* Wilcox model near the surface. The *SST* model is an improvement of the baseline *k-ω* model, taking into account the transport of the turbulent shear stress by a limitation of the eddy viscosity ν_t by

$$\nu_t = \frac{a_1 k}{\max(a_1 w, SF_2)} \tag{7}$$

where: $\nu_t = \mu_t/\rho$ and *S* represents an invariant measure of the strain rate. F_2 is a blending function, which restricts the limiter to the wall layer computed by:

$$F_2 = \tanh(\arg_2^2) \tag{8}$$

with:

$$\arg_2 = \max\left(\frac{2\sqrt{k}}{\beta' \omega y'}, \frac{500\nu}{y^2\omega}\right) \tag{9}$$

The *SST* model is a two-equation model, which means that two additional transport equations must be solved: one for the turbulent kinetic energy κ and one for the specific dissipation ω, given, respectively, by:

$$\frac{\partial(\rho k)}{\partial t} + \vec{\nabla}\cdot(\rho U k) = \vec{\nabla}\cdot\left[\left(\mu + \frac{\mu_t}{\sigma_{k3}}\right)\vec{\nabla}k\right] + P_k - \beta'\rho k\omega \tag{10}$$

$$\frac{\partial(\rho\omega)}{\partial t} + \vec{\nabla}\cdot(\rho U \omega) = \vec{\nabla}\cdot\left[\left(\mu + \frac{\mu_t}{\sigma_{\omega 3}}\right)\vec{\nabla}\omega\right] + (1-F_2)2\rho\frac{1}{\sigma_{\omega 2}\omega}\vec{\nabla}k\vec{\nabla}\omega + \alpha_3\frac{\omega}{k}P_k - \beta_3\rho\omega^2 \tag{11}$$

The constants used in the SST model equations are defined as:

$\beta' = 0.09;\ \alpha_1 = 5/9;\ \beta_1 = 0.075;\ \sigma_{k1} = 2;\ \sigma_{\omega 1} = 2;$
$\alpha_2 = 0.44;\ \beta_2 = 0.0828;\ \sigma_{k2} = 1;$ and $\sigma_{w2} = 1/0.856$

The coefficients of the SST model are a linear combination of the corresponding coefficients of the underlying models, given by:

$$\Phi_3 = F_2\Phi_1 + (1-F_2)\Phi_2 \tag{12}$$

In the transport equations, P_k is the turbulence production tensor due to viscous forces, which is computed by:

$$P_k = \mu_t\vec{\nabla}U\cdot\left(\vec{\nabla}U + \vec{\nabla}U^T\right) - \frac{2}{3}\left(\vec{\nabla}\cdot U\right)\left(3\mu_t\vec{\nabla}\cdot U + \rho k\right) \tag{13}$$

It is important to notice that the model definitions and formulation are presented as used in [20], since the numerical simulations were performed with this commercial code.

The numerical solution of the above equations involves the use of specific boundary conditions, in particular at surfaces bounding of the domain. In this study the boundary conditions were defined as function of the experimental data, as following:

Inlet: according to the experimental data, a mass flow rate of 0.011 kg/s was selected at the entrance of the solar collector. Direction of airflow was normal to air inlet. It was assumed that the air was at ambient temperature, equal to 297.2 K.

Outlet: it was assumed a gauge pressure of 0 Pa at the outlet tube.

Walls: At the walls, no slip and impermeable boundary conditions were used. These conditions assume zero tangential velocity at the walls, and a zero gradient of the other parameters in the normal direction at the walls, excepting some turbulence parameters. The temperature at the walls was set out considering the measured experimental values and applying a boundary condition of Dirichlet type. At the glass walls, the temperature was

considered equal to 35°C, and at the lower plate of the collector, the temperature was considered 57.5°C, according to experimental data. At the other plates, an adiabatic condition was assumed (zero temperature gradient in the normal direction at the wall), due to the insulation used in the prototype.

For the necessary turbulent quantities at boundaries the CFX default boundary conditions assumed for each turbulence model were employed. The models constants also were assumed as the default values considered in the CFX code. The flow is simulating considering a steady state operating condition. The air inside the dryer was assumed as an ideal gas, with an ambient pressure of 92.000 Pa. This is a characteristic ambient pressure value for Belo Horizonte, where the dryer was installed.

4. RESULTS AND DISCUSSION

The prototype of the hybrid solar dryer was experimentally tested without the trays and with no load. The airflow velocity and temperature were measured in the dryer outlet. The ambient temperature and the wall temperatures of the dryer were also measured. The ambient temperature was (297.2±2.0) K. At the time the test was performed, the measured time average temperature of the wall drying chamber was (313.7±2.0) K, of the solar absorber was (330.7±2.0) K, inside the glass collector was (308.2±2.0) K, and the outlet average temperature of the air was (311.0±2.0) K. The mass flow rate calculated at the outlet of the dryer was (0.0110±0.0005) kg/s.

The airflow inside the hybrid solar-dryer was simulated using the ANSYS-CFX 11 software package. The employed computational domain includes the dryer without the trays and without the drying products. The total number of elements and nodes varied among the different simulations and was in the range of 1.984.000 elements and 424.700 nodes. The mesh in regions near the walls was refined using the inflated boundary conditions tool of CFX 11 (Fig. 2).

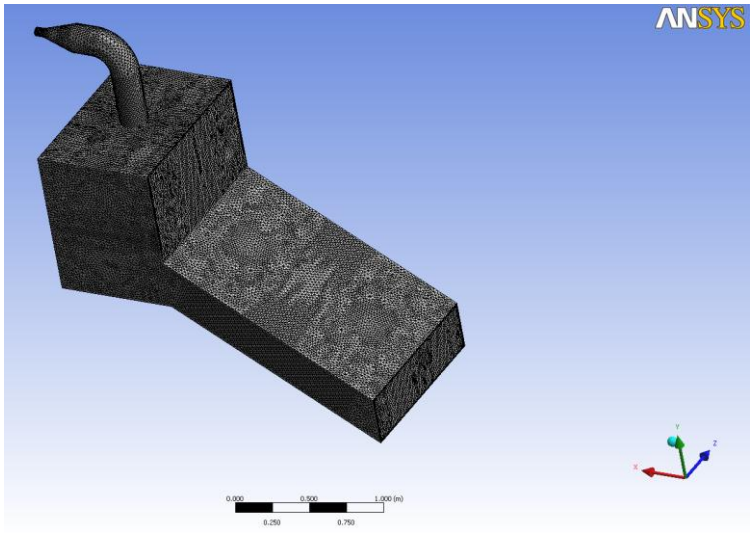

Figure 2. Surface mesh.

An Intel Core 2 Quad 2.50 GHz computer working with Windows operational system with 3.25 GB memory was used for most of the simulations, requiring about 2340 minutes of Central Processing Unit (CPU) time for the most refined mesh. The final mesh size was defined after a series of numerical tests. The control parameters were the exit average velocity and temperature, shown in Table 1.

Table 1. Settings used in a second order NMR relaxation experiment on a rock core.

Mesh	Nodes number	Exit average velocity (m/s)	Exit average temperature (K)
1	23500	3.98	308.5
2	179800	4.02	311.5
3	233000	4.02	311.7
4	287500	4.02	311.3
5	373600	4.06	311.3
6	424700	4.06	311.3

The numerically estimated outlet air temperature for the meshes 4 – 6 was 311.3 K (Table 1), which is in agreement with experimental results, inside the uncertainty range of the temperature sensors. The numerically estimated average exit velocity was 4.06 m/s for meshes 5 and 6, within the uncertainty range of the experimental value, of (4.32±0.3) m/s. The exit mass flow rate for meshes 5 and 6 is also within the uncertainty range of the experimental value. Considering these simulated values the numerical results attained a good convergence regarding the experimental data used for comparison. The numerical results presented next correspond to those obtained for the most refined mesh.

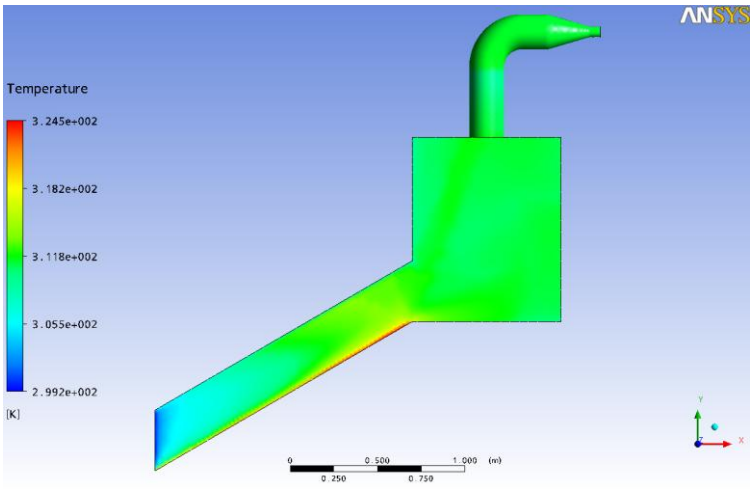

Figure 3. Wall temperatures.

Figure 3 shows the temperature field on the solar chamber and drying chamber walls (see Figure 1). It can be seen that, since the air enters the dryer at ambient temperature being heated by the solar collector, the temperature on the solar chamber walls increase towards the drying chamber. The wall temperatures are also in accordance with experimental data. The experimental value for the drying chamber wall is 313.6 K. In the simulations, a temperature of 311.6 K was obtained. It should be pointed out that these walls are well insulated in the experimental setup, and were simulated considering adiabatic wall in the numerical model. Thus the comparison considers resultant temperature values, one experimentally determined and the other numerically computed. In this case it can be noted that the model reproduces well this wall temperature.

Figure 4 presents the airflow temperature in a plane situated in the middle of the dryer (inlet section, solar chamber, drying chamber and exit region). It can be seen that the distribution of temperatures inside the dryer in this vertical plane is almost homogeneous, excepting at the solar collector surface (bottom inclined surface), where higher temperatures are obtained, of about 330 K, as well as, the highest temperature gradients. In fact this surface receives more energy than the upper surface made from glass, mainly due to the thermal radiation absorption. Overall, the mean temperature gradient between the dryer inlet and outlet regions is approximately equal to 14 K, which is a reasonable value.

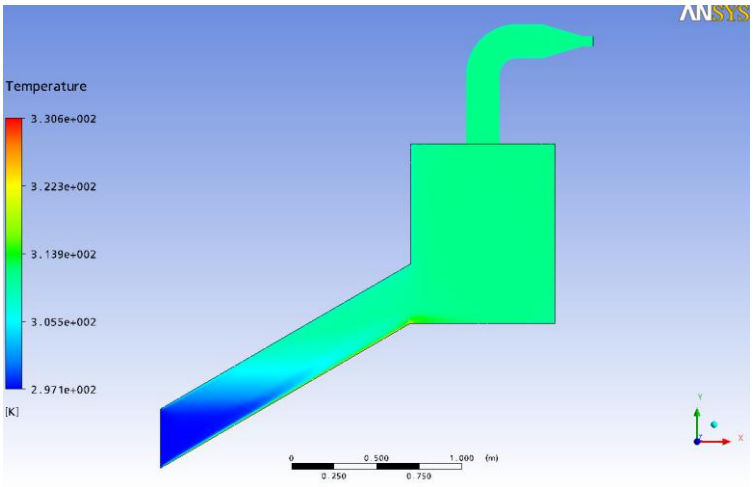

Figure 4. Temperature field inside the dryer (middle section).

In Figure 5 is shown the temperature distribution in several horizontal planes inside the drying chamber. In these cases it is observed a uniform cross-sectional distribution of the temperature field inside the drying chamber. In fact the temperatures changes more along and across the solar collector, that along and across the drying chamber. This temperature distribution is benefic, because it is expected a uniform drying processes in order to avoid different final moisture content of the products. The higher temperatures are observed at the backward wall, because in this region the flow particles coming from the solar collector more heated bottom wall circulates. It should be noted that in the present analysis the trays and the drying products were not considered leading to more uniform temperature distributions.

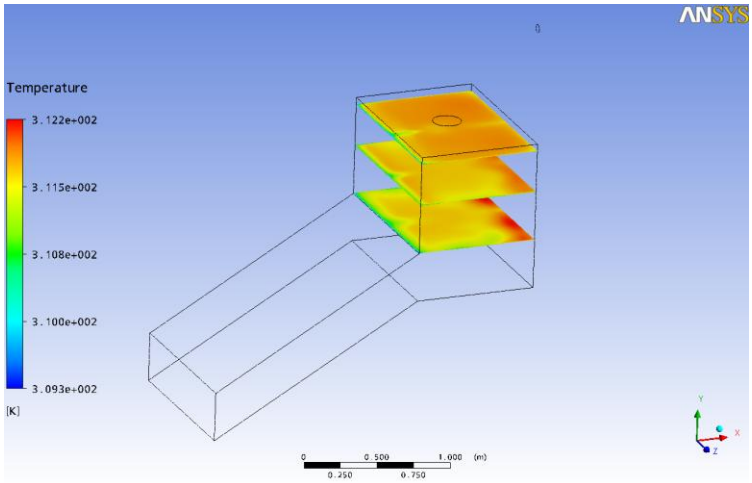

Figure 5. Temperature distribution inside the drying chamber (axis x and z directions).

Figure 6 presents the velocity field of the airflow in the middle of the dryer. The velocity increases towards the exit section. This behaviour was expected, since the flow cross-section decreases in this direction. It can also be noticed that the velocity is homogeneous in a vertical plane in the solar collector and drying chamber, denoting a small turbulent Reynolds number flow in almost all the drying section (approximately $9.0x10^3$). This behaviour of the temperature and velocity is desirable for dryer purposes, since it guarantees a high-quality and homogeneous drying process.

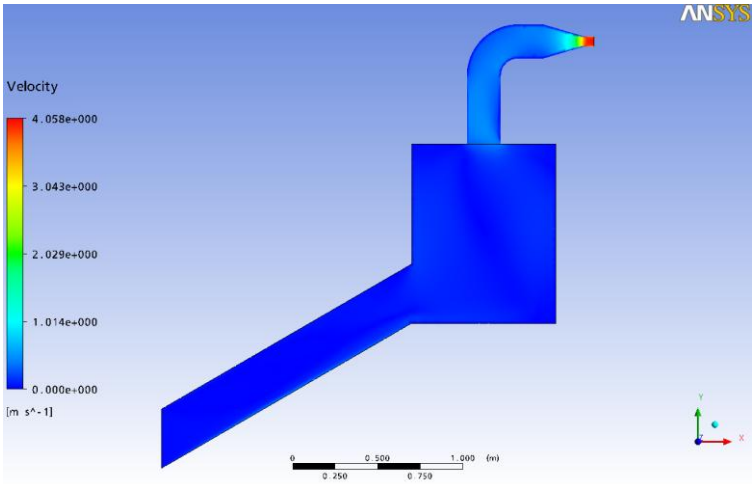

Figure 6. Velocity field inside a middle vertical plane in the dryer.

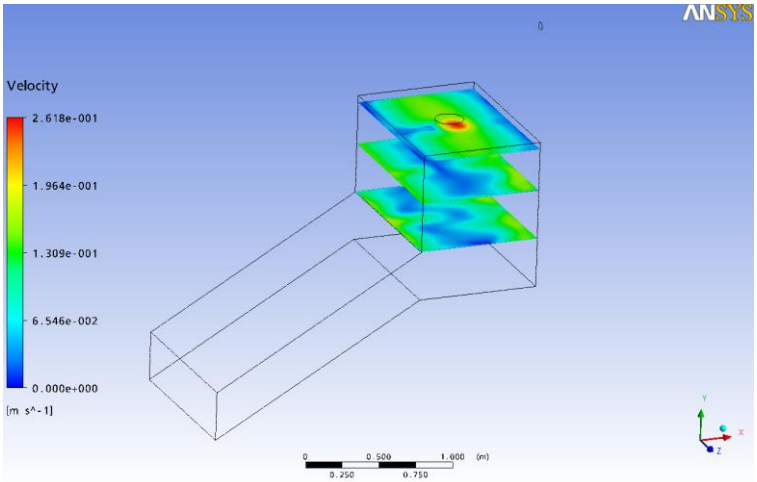

Figure 7. Mean velocity distribution inside the drying chamber.

In Figure 7 is displayed the mean velocity distribution in several cross-sectional horizontal planes inside the drying chamber. In the low lower planes in height is observed a small velocity at the drying chamber center, while in the last plane, located near the drying chamber exit the smaller velocity values are encountered at the walls. This flow pattern can be explained by the streamlines displayed in Figure 8. As observed in this figure (and previously explained in Figure 5 discussion) the hottest air coming from the solar collector bottom wall forms a recirculation region in the drying chamber vertical direction, flowing first near the drying chamber backward wall, and then turning around the others wall (top and frontal walls) of the drying chamber, finally flowing again near the backward wall to the exit region located at the top drying chamber wall. This flow pattern is the responsible by the cross-sectional temperature distribution plotted in Figure 5. Certainly other fluid particle will perform another trajectories, mainly flowing directly by the central region of the drying chamber up to the exit region. But, in average the flow behaviour above described seems to be the main flow pattern in the drying section. As expected, this recirculation region is formed by the buoyancy and forced convection effects, which are present in the flow at the same time. This flow patterns indicates that the region near the backward wall should be the more effective for drying purposes.

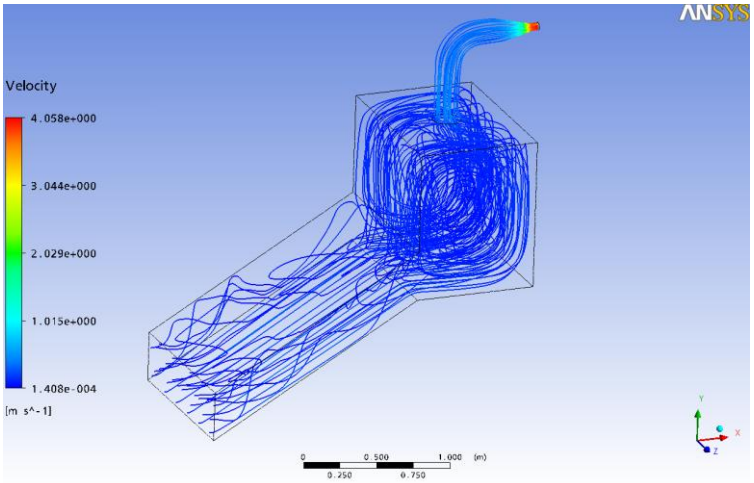

Figure 8. Flow streamlines along the solar and drying chambers.

5. OVERALL CONCLUSIONS

Hybrid solar dryers arise as an interesting option to reduce the drying costs, compared to artificial driers costs, for the same quality of the final product. In this study, a hybrid solar dryer was constructed and experimentally tested in the city of Belo Horizonte (Brazil). The dryer was tested without the trays and without any load. Steady-state temperatures and mass flow rate were measured in order to provide experimental data to validate a numerical model. The numerical simulation of the airflow inside this hybrid solar-electrical dryer was performed with the ANSYS-CFX 11 code. Experimental data was used for the boundary conditions and numerical validation. The numerical results were in agreement with experimental results, inside the uncertainty range of the temperature sensors.

The velocity and the temperature of the airflow are homogeneous in the drying chamber. This behavior is desirable and suitable for dryer purposes, since it guarantees a high-quality and homogeneous drying process. The prediction of the airflow inside the dryer can be helpful on the design of most suitable geometric configurations of the device, improving the drying process.

6. ACKNOWLEDGEMENTS

The authors are thankful to FAPEMIG (Fundo de Amparo à Pesquisa do Estado de Minas Gerais), CNPq (Conselho Nacional de Desenvolvimento Científico e Tecnológico, PUC Minas (Pontifícia Universidade Católica de Minas Gerais), CEFET-MG (Centro Federal de Educação Tecnológica de Minas Gerais) and to Uni-BH (Centro Universitário de Belo Horizonte).

7. REFERENCES

[1]. J. Prasad, V.K. Vijay, G.N. Tiwari, and V.P.S. Sorayan, Study on Performance Evaluation of Hybrid Dryer for Turmeric (Curcuma longa L.) Drying at Village Scale, *Journal of Food Engineering*. **75**, 497-502 (2006).

[2]. P. Barnwal, and G.N. Tiwari, 2008, Grape Drying by using Photovoltaic-Thermal (PV/T) Greenhouse Dryer: an Experimental Study, *Solar Energy*. **82**, 1131-1144 (2008).

[3]. J.S. Silva, "Secagem e armazenagem de produtos agrícolas". Viçosa, Aprenda Fácil (2000).

[4]. W. Mühlbauer, J. Müller, A. Esper, and M. Bux," Secagem Solar e ao Sol para Produtos Agrícolas e Florestais" (Translation to Portuguese), Universidade de Hohenheim/Instituto para Engenharia Agrícola nos Países Tropicais e Subtropicais, Stuttgart/Alemanha (1996).

[5]. B. Bena, and R.J. Fuller, Natural Convection Solar Dryer With Biomass Back-up Heater, *Solar Energy*, **72**, 75-83 (2002).

[6]. A.G. Ferreira, A.L.T. Charbel, R.L. Pires, J.G. Silva, and C.B. Maia, Analysis of a Hybrid Solar-Electrical Dryer, *Proceedings of the 19th Brazilian Congress of Mechanical Engineering*, Brazil (2007).

[7]. A. Fudholi, K. Sopian, M.H. Ruslan, M.A. Alghoul, and M.Y. Sulaiman, Review of solar dryers for agricultural and marine products, *Renewable and Sustainable Energy Reviews*, **14**, 1-30 (2010).

[8]. S. Boughali, H. Benmoussa, B. Bouchekima, D. Mennouche, H. Bouguettaia, and D. Bechki, Crop drying by indirect active hybrid solar – Electrical dryer in the eastern Algerian Septentrional Sahara, *Solar Energy*, **83,** 2223–2232 (2009).

[9]. A. Ficarella, A. Perago, G. Starace, and D. Laforgia, Thermo-fluid Dynamic Investigation of a Dryer, using Numerical and Experimental Approach, *Journal of Food Engineering*, **59,** 413-420 (2003).

[10]. S.B. Mabrouk, B. Khiari, and M. Sassi, Modelling of Heat and Mass Transfer in a Tunnel Dryer, *Applied Thermal Engineering*, **26**, 2110-2118 (2006).

[11]. S. Janjai, N. Srisittipokakun, and B.K. Bala, Experimental and Modelling Performances of a Roof-Integrated Solar Drying System for Drying Herbs and Spices, *Energy*, **33,** 91-103 (2008).

[12]. A. Kaya, O. Aydın, and I. Dincer, Experimental and numerical investigation of heat and mass transfer during drying of Hayward kiwi fruits (Actinidia Deliciosa Planch), *Journal of Food Engineering*, **88**, pp. 323–330 (2008).

[13]. Z. Naghavi, A. Moheb, and S. Ziaei-rad, Numerical simulation of rough rice drying in a deep-bed dryerusing non-equilibrium model, *Energy Conversion and Management*, **51,** 258-264 (2010).

[14]. Y. Amanlou, and A. Zomorodian, Applying CFD for designing a new fruit cabinet dryer, *Journal of Food Engineering*, **101**,.8-15 (2010).

[15]. R.J. Moffat, Describing the uncertainties in experimental results. *Experimental Thermal and Fluid Science* **1**, Issue 1, 3-17 (1988).

[16]. R.F. Menter, Two-equation Eddy-viscosity Turbulence Models for Engineering Applications. *AIAA Journal*, **32**, Issue 8, 269-289 (1994).

[17]. D.C. Wilcox, "Turbulence Modeling for CFD". DCW Industries, La Cañada, CA (1993).

[18]. B.E. Launder, and D.B. Spalding, The Numerical Computation of Turbulent Flows, *Comput. Methods Appl. Mech. Eng*., **3**, 269-289 (1974).

[19]. ANSYS-CFX®, "Solver Theory manual", Release 11.0 (2006).